PHYSICAL REVIEW B **96**, 035418 (2017)

Theoretical study of the thickness dependence of the metal-insulator transition in $Bi_2Sr_2Co_2O_8$ nanosheets

Xiaokun Huang and Weiyi Zhang
National Laboratory of Solid State Microstructures and Department of Physics, Nanjing University, Nanjing 210093, China
and Collaborative Innovation Center of Advanced Microstructures, Nanjing University, Nanjing 210093, China

(Received 14 March 2017; published 17 July 2017)

The bulk $Bi_2Sr_2Co_2O_8$ crystal is an insulator at low temperature and experiences an insulator-metal transition at $T_C \approx 60$ K. The new experiment showed that T_C increases to 140 K for a mechanically exfoliated nanosheet of four blocks and is beyond room temperature for nanosheets thinner than four blocks. We show that the thickness-dependent insulator-metal transition observed in $Bi_2Sr_2Co_2O_8$ nanosheets can naturally be explained by the strongly correlated low-spin-state insulator (LS state) and intermediate-spin-low-spin-state metal (IS-LS state). In particular, the energy difference between the LS state and IS-LS state qualitatively reproduces the trend of the transition temperature with the nanosheet thickness. The predicted transition temperature of a nanosheet with three blocks is only slightly above room temperature, a result that can be used to check our proposed mechanism. Further experiments on the distinct magnetotransport properties and spin-fluctuation behaviors of the LS state and IS-LS state are also very helpful to resolve the issue. The weak interblock binding is also consistent with the layer-resolved partial densities of states.

DOI: 10.1103/PhysRevB.96.035418

I. INTRODUCTION

Low-dimensional electronic systems often demonstrate unusual and fascinating physical properties different from their bulk counterparts. A well-known example is represented by graphene mechanically exfoliated from graphite [1]. The massless Dirac fermion dispersion near the Fermi energy makes it the most extensively studied single-atom-layer electronic system in the past decade [2]. Following the rich phenomena unveiled by the honeycomb lattice of graphene, silicene, germanene, stanene, and phosphorene, with similar structures but composed of Si, Ge, Sn, and P atoms, have also attracted much attention in the past few years [3–7]. Because of the relatively strong spin-orbit coupling in these systems, small band gaps are created at the Dirac points of graphene. Thus, novel topological insulators emerge with an electronic insulator in the bulk and a pair of helical conducting states circulating around the edge of the two-dimensional nanosheet. Recently, nanosheets composed of transition-metal sulfides, VS_2, MoS_2, and WS_2, have also been intensely studied because of their novel electronic properties [8–10]. Therefore, these layer-structured nanosheets not only offer an important platform to investigate the fascinating quantum phenomena but also lay the foundation for various device applications. This further motivated researchers to explore the properties of other possible layered systems.

More recently, nanosheets of one, two, three, and four blocks of layered $Bi_2Sr_2Co_2O_8$ are successfully prepared by Wang *et al.* using the same mechanical-exfoliation technique [11]. The transport property showed a thickness-dependent insulator-metal transition as a function of block number N. Compared with the bulk $Bi_2Sr_2Co_2O_8$ compound [12], the nanosheets manifested for the conductivity a power-law decrease with $1/N$. Generally speaking, both nanosheets and bulk $Bi_2Sr_2Co_2O_8$ showed a semiconductor or insulator behavior at low temperature. However, a thickness-dependent insulator-metal transition takes place at $T \approx 140$ K for a nanosheet with $N = 4$ but at $T \approx 60$ K for a bulk sample [12]. For nanosheets with $N < 4$, no insulator-metal transition was observed up to room temperature. The conductivities of such low-temperature insulators were explained satisfactorily using different variable-range-hopping mechanisms. However, the nature of the electronic states of both the insulator and metal of nanosheets across the insulator-metal transition temperature was not identified.

In our previous study on the transport properties of bulk $Bi_2A_2Co_2O_8$ compounds (A=Ca, Sr, Ba), we constructed the full insulator-metal phase diagram for these compounds in the parameter space of Hubbard U and the ionic radius r of atom A [13]. By sifting through different spin states of Co ions, 22 metastable magnetic structures with different spin states are obtained. The strongly correlated low-spin-state (LS-state) insulator and intermediate-spin-low-spin-state (IS-LS-state) metal turn out to be the ground-state candidates relevant for bulk $Bi_2A_2Co_2O_8$ compounds (A=Ca, Sr, Ba). In particular, we found that $Bi_2Ca_2Co_2O_8$ is deep in the insulator region and $Bi_2Ba_2Co_2O_8$ is deep in the metallic region, with $Bi_2Sr_2Co_2O_8$ as a narrow-band-gap semiconductor in the vicinity of the insulator-metal phase boundary.

In this paper, we show that the thickness-dependent insulator-metal transition observed in nanosheets can also be naturally explained by the same strongly correlated LS-state insulator and IS-LS-state metal. By calculating the electronic band structures and total energies of these two states as functions of block number, we not only reproduce qualitatively the trend of the transition temperatures for the bulk and nanosheet of $N = 4$, but we also predict the transition temperatures for other nanosheets. The insulator-metal transitions for nanosheets with $N < 4$ were not observed in previous experiments because their transition temperatures are above room temperature. Before we present our results on the thickness-dependent insulator-metal transition of nanosheets of $Bi_2Sr_2Co_2O_8$, let us first recall the mechanism behind the

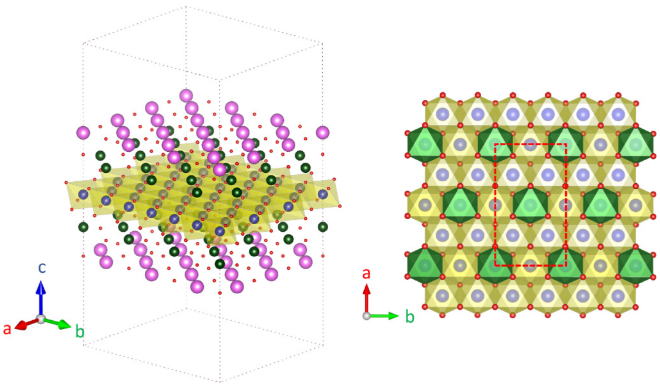

(a) (b)

FIG. 1. The crystal structure of a $Bi_2A_2Co_2O_8$ nanosheet with $N = 1$. The outer green (dark) and pink (light) spheres refer to A and Bi atoms, and the inner blue (middle) and small red spheres refer to Co and O atoms. (a) Crystal structure. (b) The extracted hexagonal structure of the CoO_2 layer viewed from the c axis. The red dashed frame denotes the double cell, in which the green CoO_2 octahedra denote the IS-Co ion embedded in the LS-Co ions background. Half of the double cell along the a axis defines the unit cell of the LS state with all Co ions in the LS state.

insulator-metal transition in bulk $Bi_2A_2Co_2O_8$ compounds (A=Ca, Sr, Ba).

As shown in Fig. 1, the crystal structure of $Bi_2A_2Co_2O_8$ (A=Ca, Sr, Ba) is characterized by the so-called composite structure in which CoO_2 forms a central layer that is symmetrically covered by rocksalt-type AO and BiO layers both above and below the CoO_2 layer [14]. This basic building block not only defines the unit cell of bulk $Bi_2A_2Co_2O_8$ but also constitutes the basic block when nanosheets are mechanically exfoliated from the bulk because the interlayer binding is weakest between the BiO layers [15]. The CoO_2 layer consists of a two-dimensional triangular lattice of Co ions, octahedrally coordinated with O ions above and below the Co plane. The formal valence of Co ions deduced from the chemical composition $Bi_2A_2Co_2O_8$ is 3+, leaving six electrons in Co $3d$ orbitals. In the edge-sharing hexagonal CoO_2 layer, the trigonal distortion of CoO_2 octahedra reduces the O_h local point group to a d_3 subgroup, in which the t_{2g} orbitals are further split into an a_{1g} singlet and an e_g' doublet [16].

Among the interesting properties observed for $Bi_2A_2Co_2O_8$ (A=Ca, Sr, Ba) [12,17–20], the most fascinating one is the insulator-metal (I-M) transition which takes place as either temperature or A's ionic radius r increases [12]. For $Bi_2Ca_2Co_2O_8$ (BCCO; $r_{Ca} = 0.99$ Å) [21] and $Bi_2Sr_2Co_2O_8$ (BSCO; $r_{Sr} = 1.13$ Å) [21], the ground states are insulators since r is small. However, they make a transition into metallic states at high temperature. The transition temperature T_C is around 140 K for $Bi_2Ca_2Co_2O_8$ and 60 K for $Bi_2Sr_2Co_2O_8$. $Bi_2Ba_2Co_2O_8$ (BBCO; $r_{Ba} = 1.35$ Å) [21] with a large r remains a metal in the whole temperature range investigated [12]. Therefore, these experiments suggested that bulk $Bi_2A_2Co_2O_8$ takes a metallic state at a larger lattice constant (high temperature), while it stays in an insulator state at a smaller lattice constant (low temperature).

The insulator-metal transition of the bulk $Bi_2A_2Co_2O_8$ is accompanied by a specific-heat peak [22]. The suppression of the specific-heat peak under a large magnetic field ($B = 13.2$ T) indicates the involvement of spin degrees of freedom [22]. This is further supported by the sizable negative magnetoresistance observed for the insulating $Bi_2Ca_2Co_2O_8$ and $Bi_2Sr_2Co_2O_8$, whereas the magnetoresistance is positive in the metallic $Bi_2Ba_2Co_2O_8$ [12]. The active role of the CoO_2 layers for the transport property is also verified by the hexagonal Fermi surface observed in the angle-resolved photoemission spectra of metallic $Bi_2Ba_2Co_2O_8$ [23–25].

The spin-fluctuation involvement reminds us of the spin-state transition of Co^{+3} ions. It is well known that the Co d orbitals of perovskite $LaCoO_3$ are decomposed into a t_{2g} triplet (xy, yz, zx) and e_g doublet (x^2-y^2, $3z^2-r^2$) separated by a crystal-field-splitting $10Dq$ [26,27]. Depending on the competition between Hund's rule coupling J_H and the crystal-field-splitting energy $10Dq$, a low-spin ($t_{2g}^6e_g^0$, $S = 0$), intermediate-spin ($t_{2g}^5e_g^1$, $S = 1$), or high-spin (HS; $t_{2g}^4e_g^2$, $S = 2$) state is a possible candidate [26–29]. In particular, $10Dq$ can easily be tuned either by the ionic radius or temperature since it is inversely proportional to the fifth power of the lattice constant. The insulator-metal transition in bulk $Bi_2A_2Co_2O_8$ has an origin similar to that of the spin-state transition in $LaCoO_3$ [26–29]. The derived insulator-metal phase diagram shows that the strongly correlated LS-state insulator and the hexagonally arranged IS-LS-state metal are part of a consistent description of the physical properties of bulk $Bi_2A_2Co_2O_8$ both below and above the transition temperature. It also explains the insulator-metal transition separating $Bi_2Ca_2Co_2O_8$, $Bi_2Sr_2Co_2O_8$, and $Bi_2Ba_2Co_2O_8$ [13].

However, the spin-state transitions in $LaCoO_3$ and $Bi_2A_2Co_2O_8$ also differ in the following two fundamental aspects. First, the IS state is not favored in the prototype spin-state transition compound $LaCoO_3$ because of the more energy favorable LS-HS state, as pointed out in Refs. [27,30]. The IS-LS state is made possible in $Bi_2A_2Co_2O_8$ because of the rocksalt layers situated both above and below the CoO_2 layers. Unlike the LS-state insulator of $LaCoO_3$, the band gap occurs between the Co $d(t_{2g})$-derived valence bands and Co $d(e_g)$-derived conduction bands due to the crystal-field splitting. The LS-state insulator of $Bi_2A_2Co_2O_8$ takes place between the Co $d(t_{2g})$-derived valence bands and Bi p-derived conduction bands because Bi p orbitals are much lower in energy than the Co $d(e_g)$ orbitals. The IS-LS-state metal becomes possible since the virtual excitation energy for spin-state transition is significantly reduced. Second, the LS state becomes an insulator in $Bi_2A_2Co_2O_8$ only when Hubbard U on Co ions is large; thus, we call it the strongly correlated LS-state insulator for the LS state [13].

Using the material parameters of bulk $Bi_2Sr_2Co_2O_8$ extracted from the previously obtained insulator-metal phase diagram [13], we systematically study the thickness-dependent insulator-metal transition observed in $Bi_2Sr_2Co_2O_8$ nanosheets. We first make sure that the strongly correlated LS-state insulator and the IS-LS-state metal remain the best candidates for the ground states of $Bi_2Sr_2Co_2O_8$. Then we calculate the self-consistent electronic band structures and total energies of both states for nanosheets with $1 \leqslant N \leqslant 4$

and compare the results with those of the bulk compound. The energy difference of these two states for each nanosheet can be converted into the insulator-metal transition temperature by scaling it to that of the bulk compound. Thus, a qualitative comparison of transition temperatures can be made between the theoretically predicted and experimentally measured values of nanosheets. The band structures of the LS-state insulator, in particular the size of the band gaps, are directly related to the corresponding electric conductivities at low temperature, whose trend is also discussed with regard to the experiment. Our layer-resolved partial densities of states (PDOSs) will also show that the electronic structure at the surface atomic layers slightly differs from those of the bulk, whereas those of the inner atomic layers of thick nanosheets remain as in the bulk. This is also the physical reason why the thickness-dependent transition temperature of nanosheets quickly approaches the bulk value when the block number exceeds 4. The small differences of PDOSs between the surface and inner atomic layers also suggest that $Bi_2Sr_2Co_2O_8$ is a truly layered compound, and mechanical exfoliation of nanosheets is a reflection of such a feature.

The rest of the paper is organized in the following way. In Sec. II, we first briefly describe the density-functional theory and the relevant parameter setting for the calculations of our nanosheets. Then the total energies and electronic structures are presented for nanosheets of one to four blocks. The converted thickness-dependent transition temperatures are deducted and compared with measured values. The physical mechanism involved in the insulator-metal transition is discussed using the layer-resolved PDOSs. Conclusions are drawn in Sec. III.

II. RESULTS AND DISCUSSIONS

The electronic structures are calculated using a plane-wave pseudopotential approach to the density-functional theory as implemented in the Vienna Ab initio Simulation Package (VASP 5.3.5) [31,32]. The Ceperley-Alder functional is used as the exchange-correlation potential [33]. The projector augmented-wave potentials explicitly include 10 valence electrons for Sr ($3s^23p^64s^2$), 17 for Co ($3s^23p^63d^84s^1$), 5 for Bi ($6s^26p^3$), and 6 for O ($2s^22p^4$). The rotationally invariant local spin-density approximation (LSDA) + U approach introduced by Liechtenstein *et al.* was adopted for Co 3d orbitals with the double counting explicitly subtracted [34]. The wave functions are expanded using a plane-wave basis with an energy cutoff of 600 eV. The $8 \times 8 \times 1$ and $4 \times 8 \times 1$ Monkhorst-Pack k-point meshes are used for the unit cell of the nanosheets with N blocks $[(Bi_2Sr_2O_4)_2(CoO_2)_4]_N$ [half of the rectangular frame of Fig. 1(b), 28N atoms] and the double cell [the full rectangular frame of Fig. 1(b), 56N atoms], respectively [35]. The $8 \times 8 \times 2$ and $4 \times 8 \times 2$ Monkhorst-Pack k-point meshes are used for the bulk $(Bi_2Sr_2O_4)_2(CoO_2)_4$ unit cell and the double cell, respectively. The total energies and densities of states (DOSs) of nanosheets are calculated using the linear tetrahedron method with Bloch corrections [36]. Each self-consistent electronic calculation is converged to 10^{-5} eV, and the tolerance force is set to 0.01 eV/Å for the relaxation of the atomic positions. As is usually done for a late transition-metal element such as Co, the Hund's rule coupling J_H is fixed at 1 eV [37], while the on-site Hubbard U is set at 7.6 eV, as was suggested by the phase diagram of bulk $Bi_2A_2Co_2O_8$ (A=Ca, Sr, Ba) [13]. As is well known, the LSDA+U approach, similar to the unrestricted Hartree-Fock approximation, is one of the most straightforward and well-defined approximations. It gives, as a first-order approximation, qualitatively correct results, although the insulating gap is usually somewhat overestimated. LSDA+U is usually able to offer reliable total energy of a compound but not the quasiparticle spectrum if strong correlation is involved among electrons. Thus, our predicted insulator-metal transition temperature should be reliable since it involves only the energy difference between the LS-state insulator and IS-LS-state metal. But the exact band-gap size of the LS-state insulator and the quasiparticle spectra of the IS-LS-state metal should be handled with caution.

The initial crystal structures of nanosheets are constructed from the P-1 crystal phase of bulk $Bi_2Sr_2Co_2O_8$ [13]. The nanosheets are N blocks thick (see Fig. 1), stacked along the c axis and separated by a 1.5-nm vacuum spacer. The supercells are composed of 28N atoms for single and 56N atoms for double in-plane unit cells. The supercells are then fully relaxed both structurally and electronically for different magnetic structures to optimize their energies. To make sure the insulator-metal transition takes place among the same quantum states as in the bulk, we first check the hierarchy of the 22 magnetic structures in nanosheets. The sequence of those lowest-energy states remains the same, thus ensuring that the relevant electronic states are still the strongly correlated LS-state insulator and the IS-LS-state metal as illustrated in Fig. 1(b). In the following, we mainly concentrate on these two electronic states.

With the parameters given above and the procedure outlined, the electronic structures and total energies of $Bi_2Sr_2Co_2O_8$ nanosheets ($N = 1$–4) are calculated for both the LS state and the IS-LS state together with those of the bulk. To facilitate a comparison between different electronic states and between nanosheets with different N, all energies are presented in terms of a single-block double cell [see Fig. 1(b), 56 atoms]. In Fig. 2, the energy difference per double cell $\Delta E = E_{IS-LS} - E_{LS}$ between the LS state and the IS-LS state is plotted as a function of $1/N$. The corresponding energies of the LS state (E_{LS}) and IS-LS state (E_{IS-LS}) are also shown in the inset. Although the energy of each state demonstrates an approximately linear increasing behavior with $1/N$ and reveals an enhanced binding energy with increasing nanosheet thickness, the energy difference unveils a rather nonlinear feature with $1/N$, showing a clear dimensional-crossover pattern from three-dimensional to two-dimensional (2D) systems. The nanosheets with $1 < N < 3$ can be classified as 2D systems due to their proximity in energy, whereas the nanosheets with $3 < N < 6$ can be viewed as a crossover region because of the steep energy drop. The thick nanosheets with $N > 10$ are already very close to the bulk compound ($N \rightarrow \infty$). The nanosheet with $N = 4$ is what we can still manage numerically; the case with $N = 5$ is already beyond our computational capability. As can be seen from the inset of Fig. 2, the steep drop in the energy difference is mainly caused by a deviation of the LS state in the crossover region. Detailed analysis suggests that the sudden change is associated with a

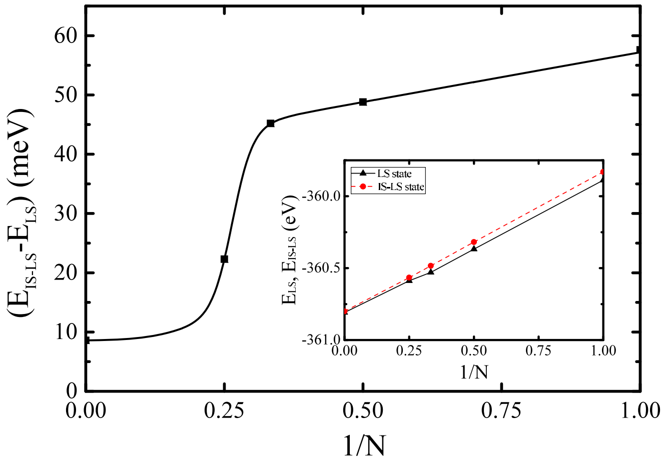

FIG. 2. The energy difference $\Delta E = E_{IS-LS} - E_{LS}$ per double cell as a function of $1/N$. The inset plots E_{IS-LS} and E_{LS} per double cell as a function of $1/N$. The symbols are the data points, and the lines are only to guide the eyes.

pseudo-Jahn-Teller effect of the specific nanosheets [38]. As suggested in our previous study on the bulk compounds, the insulator-metal transition takes place between the LS state and IS-LS state. Thus, the transition temperature should scale with this energy difference. The calculated ΔE are 57.6, 48.8, 45.2, 22.3, and 8.6 meV for nanosheets $N = 1,2,3,4$ and the bulk, while their converted transition temperatures are $T_C = 402$, 340, 315, 156, and 60 K, respectively, if we take the bulk $T_C = 60$ K as a reference. Therefore, the deducted T_C for a nanosheet with $N = 4$ is very close to the observed value of 140 K. The estimated value for a nanosheet with $N = 3$ is 315 K, only slightly above room temperature. This prediction can be used as a smoking gun to check the physical mechanism we propose.

To explore the evolution of nanosheets with nanosheet thickness, the band structures are presented in Fig. 3 for both the LS state and IS-LS state. Band dispersions are plotted along the high-symmetry points $X(\frac{1}{2}00)$, $\Gamma(000)$, $Y(0\frac{1}{2}0)$, $L(\frac{1}{2}\frac{1}{2}0)$, and $\Gamma(000)$ in the irreducible Brillouin zone. The conduction bands are contributed by BiO layers, while the valence bands originate from the CoO_2 layers. Figure 3 shows that the LS state is always an indirect band-gap insulator irrespective of nanosheet thickness, while the IS-LS state is always a spin-polarized semimetal due to the overlap between the conduction bands and majority-spin valence bands. Let us first analyze the electronic structures of the LS state. The two lowest conduction bands of nanosheet $N = 1$ are each of degeneracy 2 and are both derived from two surface BiO layers. When the nanosheet thickness is doubled, two extra conduction bands emerge around each of the original bands of nanosheet $N = 1$. These bands are split from the coupled inner BiO-BiO layers. As the nanosheet-thickness increases, the degeneracy of these split bands increases accordingly while keeping the original bands of surface BiO layers intact. When $N \to \infty$, the surface BiO layers disappear and so do their contributed bands. This is clearly illustrated in the right panel of Fig. 3 for the bulk compound. Since the valence bands all come from the inner CoO_2 layers, the band structures of the LS state are all similar, except the band degeneracy, which increases proportional to N. The above analysis applies also to the band structures of the IS-LS state. One sees that the overall pattern of the valence bands is quite similar, except for the proportionally increased degeneracy. Concerning the LS state, one notices that the insulator gap decreases almost monotonically with nanosheet thickness, with the bulk having

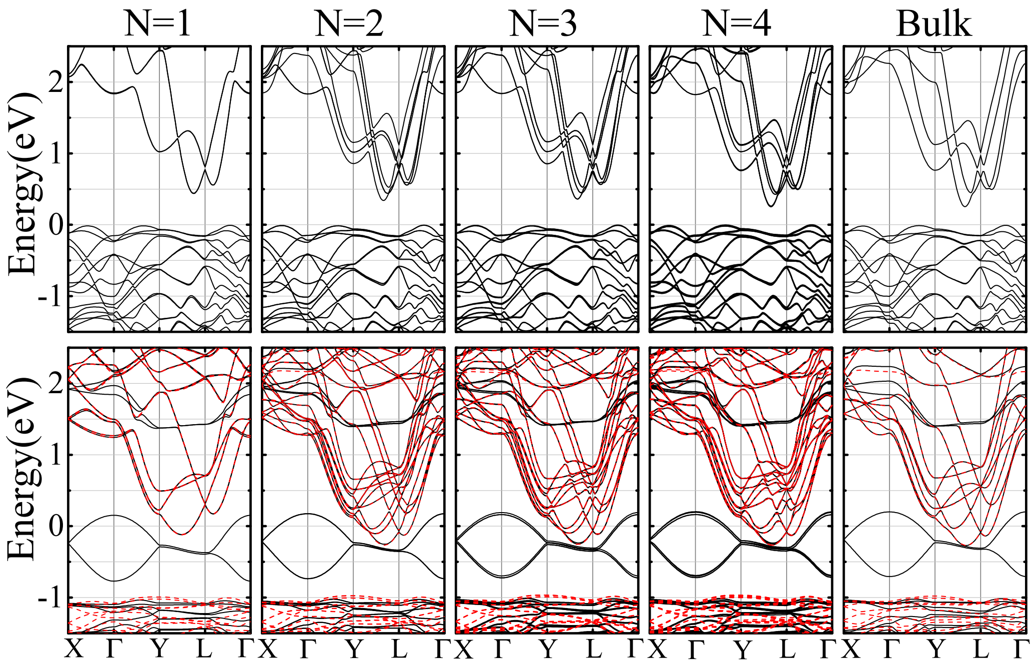

FIG. 3. The electronic band structures of the LS state and the IS-LS state. The top panel represents the LS-state insulator, while the bottom panel represents the IS-LS-state metal. From left to right are the nanosheets for $N = 1,2,3,4$ and the bulk compound. The black solid lines refer to majority-spin bands, and red dashed lines refer to minority-spin bands of the IS-LS state.

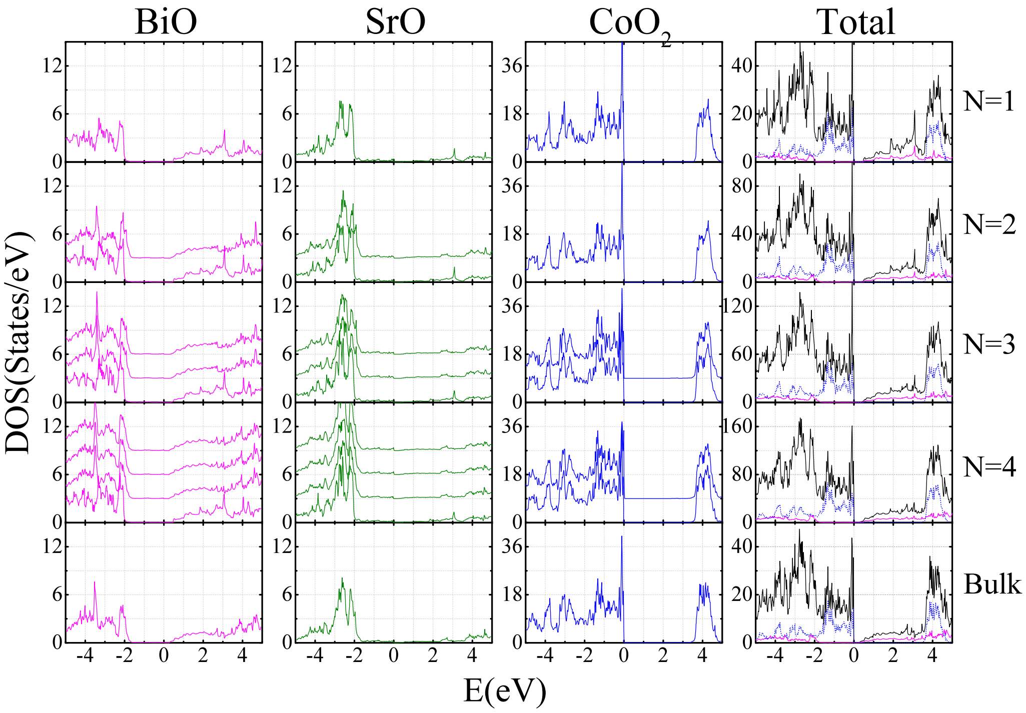

FIG. 4. The layer-resolved densities of states of the LS state of $Bi_2Sr_2Co_2O_8$ nanosheets. From top to bottom are the nanosheets for $N = 1,2,3,4$ and the bulk. The PDOSs are plotted from left to right for the BiO, SrO, and CoO_2 layers and the TDOS. For each pair of BiO, SrO, and CoO_2 layers which are symmetrical with respect to the center of nanosheet, only one of them is displayed. The PDOSs of the different labeled regions with the same composition are plotted together with incremented offsets from the outer to inner layers. Plotted together with TDOS (black solid lines) are the Bi-resolved (pink dotted lines) and Co-resolved (blue dashed lines) PDOSs.

the smallest band gap. The insulator gap decreases slightly with N because of the enhanced Bi p-derived conduction bands brought about by the reduced bond length between inner BiO-BiO layers. This trend is in agreement with the resistivity measurements on nanosheets [11]. As for the IS-LS state, a similar mechanism holds. The valence and conduction bands are closer to each other as the nanosheet thickness increases, indicating improved conductivity with nanosheet thickness above the transition temperature.

The reason why $Bi_2Sr_2Co_2O_8$ nanosheets can easily be made using the mechanical-exfoliation technique can be understood from the layer-resolved PDOSs presented in Fig. 4. To facilitate a systematic comparison between different nanosheets and between different atomic regions, the DOSs of nanosheets $N = 1,2,3,4$ and the bulk compound are displayed from the top to bottom, while the PDOSs of BiO, SrO, and CoO_2 layers and the total DOS (TDOS) are shown from left to right. The PDOSs of different atomic regions corresponding to the same composition are drawn in the same subplot with incremental positive offset for easier viewing. For the BiO atomic region which appears both as surface layers and inner layers of the nanosheets, the PDOS of the surface layers differs slightly from those of the inner layers. The surface bands are also narrower than the inner bands. However, the inner PDOSs are almost the same irrespective of their position away from the surface. Such a conclusion is also valid for the SrO atomic region. It is seen that only the atomic layers closest to the surfaces differ slightly from the inner layers, while all inner atomic layers remain almost the same irrespective of the thickness of the nanosheets. This suggests that the surface only slightly affects the first two rocksalt atomic layers. The weak binding between different atomic layers facilitates the mechanical-exfoliation technique. As for the CoO_2 layers, two atomic layers away from the surface, the PDOSs show almost no difference, which further confirms the short-range impact of surfaces on the electronic states. The PDOSs and TDOSs also clearly show that the band gap occurs between the BiO-derived conduction bands and CoO_2-derived valence bands in the LS-state insulator. The band gap only weakly depends on and slightly shrinks with increased nanosheet thickness.

To understand the metallic property of the nanosheets above the insulator-metal transition temperature, it is worthwhile to investigate the layer-resolved PDOSs of the IS-LS state of $Bi_2Sr_2Co_2O_8$ nanosheets. As illustrated in Fig. 5, the IS-LS state is a ferrimagnetic semimetal due to the spin-state transition of Co ions. The averaged magnetic moment is $0.46\mu_B/\mathrm{Co}$. The magnetic coupling between IS-Co ions is expected to be weak because of the intervening LS-Co ions. The charge carriers involve both electrons at the bottom of the BiO-derived conduction bands and holes at the top of CoO_2-derived valence bands. Similar to those of the LS state, only the PDOSs of the first two atomic layers near the surface have a slight difference from the inner ones, while all inner PDOSs of the same atomic compositions are almost indistinguishable from each other. As revealed by the electronic band structures, the layer-resolved PDOSs of the bulk compound are very close to those of inner atomic layers, as should be the case. The other common feature is that the electronic states in the surface layers are less extended than

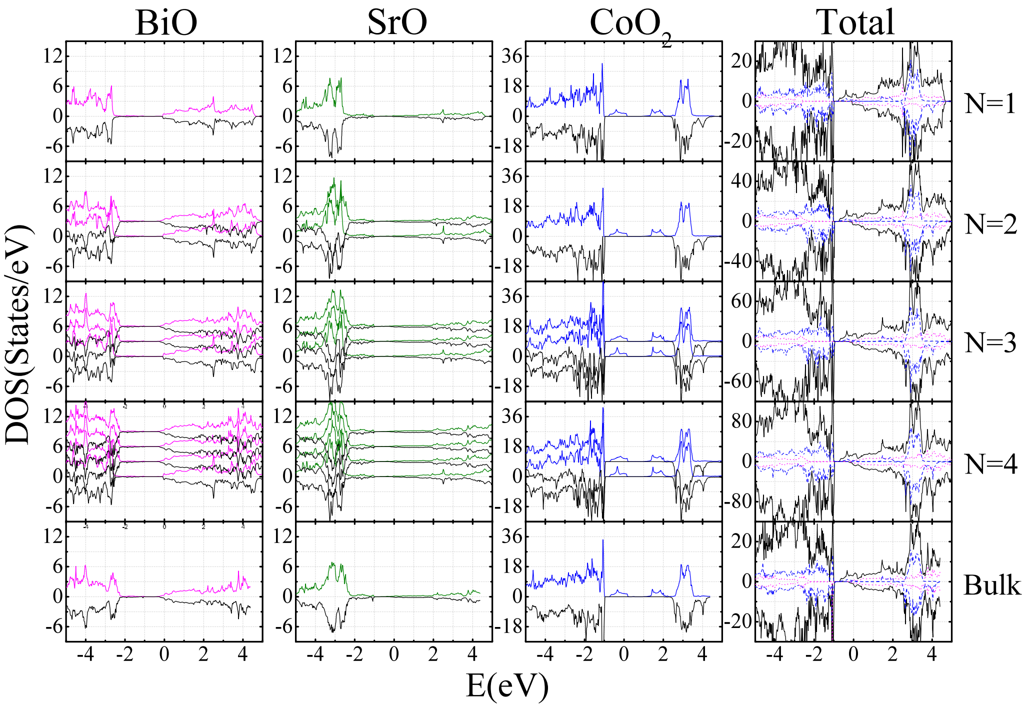

FIG. 5. The layer-resolved densities of states of the IS-LS state of $Bi_2Sr_2Co_2O_8$ nanosheets. From top to bottom are the nanosheets for $N = 1,2,3,4$ and the bulk. The PDOSs are plotted from left to right for the BiO, SrO, and CoO_2 layers and the TDOS. For each pair of BiO, SrO, and CoO_2 layers which are symmetrical with respect to the center of nanosheet, only one of them is displayed. The PDOSs of the different labeled regions with the same composition are plotted together with incremented offsets from the outer to inner layers. Plotted together with TDOS (black solid lines) are the Bi-resolved (pink dotted lines) and Co-resolved (blue dashed lines) PDOSs. As usual, the DOSs of majority spin are plotted upwards (positive offsets), while those of minority-spin are plotted downwards (negative offsets).

those of the inner atomic layers, reflecting a slightly enhanced binding of the inner layers.

Comparative studies have also been done for the $Bi_2Ca_2Co_2O_8$ and $Bi_2Ba_2Co_2O_8$ compounds. They are not presented here because $Bi_2Ca_2Co_2O_8$ nanosheets are deep in the insulator region and the required insulator-metal transition temperature is unrealistically higher than room temperature. The $Bi_2Ba_2Co_2O_8$ nanosheets are deep in the metallic region without an insulator-metal transition.

III. CONCLUSION

In summary, the thickness-dependent insulator-metal transition of $Bi_2Sr_2Co_2O_8$ nanosheets was systematically studied in this paper. Our proposed LS-state insulator and IS-LS-state metal reproduce the low-temperature insulating and high-temperature metallic phases for the bulk and a nanosheet of four blocks. We also predict that the insulator-metal transition temperature of a nanosheet with $N = 3$ is only slightly above room temperature, which can be checked by further measurements on the existing samples. In addition, the spin fluctuation is anticipated in the high-temperature IS-LS state, while it is frozen in the low-temperature LS state. These distinct behaviors are surely reflected in the thermodynamical and thermoelectric properties associated with the spin entropy of Co ions, as was observed in water-intercalated Na_xCoO_2 superconductors [39–41] and the half-doped $Na_{1/2}CoO_2$ compound [42–44]. More experiments on $Bi_2Sr_2Co_2O_8$ nanosheets are surely required to validate or invalidate the mechanism proposed in this paper.

ACKNOWLEDGMENTS

This work was supported in part by the NNSFC under Grant No. 11474148. Part of the numerical calculations was carried out in the High Performance Computing Center (HPCC) of Nanjing University. We are also grateful to both referees for their constructive suggestions and for the wonderful English polishing of our manuscript by the second referee.

---

[1] K. S. Novoselov, A. K. Geim, S. V. Morozov, D. Jiang, Y. Zhang, S. V. Dubonos, I. V. Grigorieva, and A. A. Firsov, Science **306**, 666 (2004).

[2] A. H. Castro Neto, F. Guinea, N. M. R. Peres, K. S. Novoselov, and A. K. Geim, Rev. Mod. Phys. **81**, 109 (2009).

[3] M. Ezawa, J. Phys. Soc. Jpn. **84**, 121003 (2015).

[4] B. Lalmi, H. Oughaddou, H. Enriquez, A. Kara, S. Vizzini, B. Ealet, and B. Aufray, Appl. Phys. Lett. **97**, 223109 (2010).

[5] M. E. Dávila, L. Xian, S. Cahangirov, A. Rubio, and G. Le Lay, New J. Phys. **16**, 095002 (2014).

[6] F. F. Zhu, W. J. Chen, Y. Xu, C. L. Gao, D. D. Guan, C. H. Liu, D. Qian, S. C. Zhang, and J. F. Jia, Nat. Mater. **14**, 1020 (2015).

[7] H. Liu, A. T. Neal, Z. Zhu, Z. Luo, X. Xu, D. Tománek, and P. D. Ye, ACS Nano **8**, 4033 (2014).

[8] J. Feng, X. Sun, C. Wu, L. Peng, C. Lin, S. Hu, J. Yang, and Y. Xie, J. Am. Chem. Soc. **133**, 17832 (2011).

[9] K. F. Mak, C. Lee, J. Hone, J. Shan, and T. F. Heinz, Phys. Rev. Lett. **105**, 136805 (2010).

[10] Q. H. Wang, K. Kalantar-Zadeh, A. Kis, J. N. Coleman, and M. S. Strano, Nat. Nanotechnol. **7**, 699 (2012).

[11] Y. Wang, R. Cheng, J. Dong, Y. Liu, H. Zhou, W. J. Yu, I. Terasaki, Y. Huang, and X. Duan, APL Mater. **2**, 092507 (2014).

[12] S. T. Dong, B. B. Zhang, L. Y. Zhang, Y. B. Chen, S. H. Yao, J. Zhou, S. T. Zhang, Z. B. Gu, and Y. F. Chen, Appl. Phys. Lett. **105**, 042105 (2014).

[13] X. K. Huang and W. Y. Zhang, Sci. Rep. **6**, 38212 (2016).

[14] H. Leligny, D. Grebille, O. Pérez, A. C. Masset, M. Hervieu, and B. Raveau, Acta Crystallogr. Sect. B **56**, 173 (2000).

[15] J. D. Baran, D. Kepaptsoglou, M. Molinari, N. Kulwongwit, F. Azough, R. Freer, Q. M. Ramasse, and S. C. Parker, Chem. Mater. **28**, 7470 (2016).

[16] D. J. Singh, Phys. Rev. B **61**, 13397 (2000).

[17] R. Funahashi and M. Shikano, Appl. Phys. Lett. **81**, 1459 (2002).

[18] A. Maignan, S. Hébert, M. Hervieu, C. Michel, D. Pelloquin, and D. Khomskii, J. Phys. Condens. Matter. **15**, 2711 (2003).

[19] M. Hervieu, A. Maignan, C. Michel, V. Hardy, N. Créon, and B. Raveau, Phys. Rev. B **67**, 045112 (2003).

[20] J. Sugiyama, Y. Ikedo, H. Nozaki, P. L. Russo, J. H. Brewer, E. J. Ansaldo, G. D. Morris, K. H. Chow, S. L. Stubbs, D. Andreica, A. Amato, T. Fujii, S. Okada, and I. Terasaki, Phys. Rev. B **78**, 094422 (2008).

[21] L. Pauling, *The Nature of the Chemical Bond*, 3rd ed. (Cornell University Press, Ithaca, NY, 1960), p. 514.

[22] T. Yamamoto, K. Uchinokura, and I. Tsukada, Phys. Rev. B **65**, 184434 (2002).

[23] V. Brouet, A. Nicolaou, M. Zacchigna, A. Tejeda, L. Patthey, S. Hébert, W. Kobayashi, H. Muguerra, and D. Grebille, Phys. Rev. B **76**, 100403(R) (2007).

[24] A. Nicolaou, V. Brouet, M. Zacchigna, I. Vobornik, A. Tejeda, A. Taleb-Ibrahimi, P. Le Fèvre, F. Bertran, C. Chambon, S. Kubsky, S. Hébert, H. Muguerra, and D. Grebille, Europhys. Lett. **89**, 37010 (2010).

[25] A. Nicolaou, V. Brouet, M. Zacchigna, I. Vobornik, A. Tejeda, A. Taleb-Ibrahimi, P. Le Fèvre, F. Bertran, S. Hébert, H. Muguerra, and D. Grebille, Phys. Rev. Lett. **104**, 056403 (2010).

[26] M. Abbate, J. C. Fuggle, A. Fujimori, L. H. Tjeng, C. T. Chen, R. Potze, G. A. Sawatzky, H. Eisaki, and S. Uchida, Phys. Rev. B **47**, 16124 (1993).

[27] M. Zhuang, W. Y. Zhang, and N. B. Ming, Phys. Rev. B **57**, 10705 (1998).

[28] Y. Tokura, Y. Okimoto, S. Yamaguchi, H. Taniguchi, T. Kimura, and H. Takagi, Phys. Rev. B **58**, R1699 (1998).

[29] A. Podlesnyak, S. Streule, J. Mesot, M. Medarde, E. Pomjakushina, K. Conder, A. Tanaka, M. W. Haverkort, and D. I. Khomskii, Phys. Rev. Lett. **97**, 247208 (2006).

[30] G. R. Zhang, E. Gorelov, E. Koch, and E. Pavarini, Phys. Rev. B **86**, 184413 (2012).

[31] G. Kresse and J. Hafner, Phys. Rev. B **47**, 558 (1993).

[32] G. Kresse and J. Furthmüller, Phys. Rev. B **54**, 11169 (1996).

[33] D. M. Ceperley and B. J. Alder, Phys. Rev. Lett. **45**, 566 (1980).

[34] A. I. Liechtenstein, V. I. Anisimov, and J. Zaanen, Phys. Rev. B **52**, R5467 (1995).

[35] H. J. Monkhorst and J. D. Pack, Phys. Rev. B **13**, 5188 (1976).

[36] P. E. Blöchl, O. Jepsen, and O. K. Andersen, Phys. Rev. B **49**, 16223 (1994).

[37] I. Solovyev, N. Hamada, and K. Terakura, Phys. Rev. B **53**, 7158 (1996).

[38] I. B. Bersuker, Phys. Lett. **20**, 589 (1966).

[39] A. C. Masset, C. Michel, A. Maignan, M. Hervieu, O. Toulemonde, F. Studer, B. Raveau, and J. Hejtmanek, Phys. Rev. B **62**, 166 (2000).

[40] K. Takada, H. Sakurai, E. Takayama-Muromachi, F. Izumi, R. A. Dilanian, and T. Sasaki, Nature (London) **422**, 53 (2003).

[41] R. Schaak, T. Klimczuk, M. L. Foo, and R. J. Cava, Nature (London) **424**, 527 (2003).

[42] I. Terasaki, Y. Sasago, and K. Uchinokura, Phys. Rev. B **56**, R12685 (1997).

[43] W. Koshibae, K. Tsutsui, and S. Maekawa, Phys. Rev. B **62**, 6869 (2000).

[44] Y. Wang, N. S. Rogado, R. J. Cava, and N. P. Ong, Nature (London) **423**, 425 (2003).